Chemical Engineering Journal 478 (2023) 147387

Contents lists available at ScienceDirect

Chemical Engineering Journal

journal homepage: www.elsevier.com/locate/cej

2D transition metal carbides trigger enhanced dehydrogenation and reversibility properties in $Mg(BH_4)_2$

Yujie Lv [a], Yifan Jing [e], Bao Zhang [b,c], Yingxue Li [d], Guanglin Xia [d], Xuebin Yu [d], Pengru Huang [e], Haixiang Huang [a], Bogu Liu [b], Jianguang Yuan [b,c], Ying Wu [a,b,*]

[a] School of Energy Power and Mechanical Engineering, North China Electric Power University, No.2 Beinonglu, Changping District, Beijing 102206, China
[b] Institute of Energy Power Innovation, North China Electric Power University, No.2 Beinonglu, Changping District, Beijing 102206, China
[c] Jiangsu JITRI Advanced Energy & Materials Research Institute Co., Ltd. No.5 Chongyinanlu, Xingbei District, Changzhou 213000, China
[d] Department of Materials Science, Fudan University, Shanghai 200433, China
[e] School of Material Science & Engineering, Guangxi Key Laboratory of Information Materials and Guangxi Collaborative Innovation Center of Structure and Property for New Energy and Materials, Guilin University of Electronic Technology, Guilin 541004, China

ARTICLE INFO

Keywords:
Hydrogen storage
$Mg(BH_4)_2$
MXene
Catalyst
DFT calculation

ABSTRACT

Although $Mg(BH_4)_2$ has been widely studied in the hydrogen storage field for its high hydrogen density, its terrible dehydriding kinetics and cycling features remain impediments to practical applications. Herein, introducing different MXenes (Ti_3C_2, Ti_2C, Nb_2C) with novel two-dimensional structures as catalysts into $Mg(BH_4)_2$ has been demonstrated to be an efficient approach to boosting the hydrogen storage properties. 30 wt% MXenes in $Mg(BH_4)_2$ causes a considerable reduction in its hydrogen release temperature, remarkable increases in its dehydrogenation rate and capacity, and an enhancement to its reversibility. The $Mg(BH_4)_2$-30Ti_2C as the most excellent composite starts to liberate hydrogen from 132 °C, 143 °C lower than that of $Mg(BH_4)_2$. Furthermore, at 260 °C, the $Mg(BH_4)_2$-30Ti_2C composite desorbs 10.2 wt% H_2, which is much higher than that of $Mg(BH_4)_2$ (1.5 wt%). Theoretical calculations elucidate the weakening of B-H bonds caused by the electron transfer at the Mg$(BH_4)_2$/MXenes interfaces, and the dehybridization effect between the B and H orbits. X-ray photoelectron spectroscopy (XPS) analyses prove the *in-situ* formation of multiphase interfaces resulting from the interaction of $Mg(BH_4)_2$ and MXenes during milling and dehydrogenation processes, which could increase electron conduction and facilitate hydrogen diffusion. These factors contribute to the outstanding dehydrogenation properties of Mg$(BH_4)_2$.

1. Introduction

Under the background of the global energy crisis and environmental issues, hydrogen is widely believed to be a very promising alternative to fossil fuels in view of its cleanliness and renewability [1,2]. However, the deficiency of solutions to secure and high-efficiency hydrogen storage and transportation is an urgent problem, which has been limiting its large-scale applications. Currently, high-pressure compression and low-temperature liquefaction are prevalent methods to store hydrogen [3]. While the solid-state hydrogen storage technology, which stores hydrogen in various solid materials through physisorption and (or) chemisorption, shows significant advantages concerning safety and efficiency [4,5]. Factors such as H_2 density, dehydrogenation/rehydrogenation conditions mainly including temperature and H_2 pressure, and reversible H_2 capacity need to be comprehensively considered when choosing suitable materials for hydrogen storage applications. $Mg(BH_4)_2$ is deemed a potential candidate for the very large H_2 capacities (weight-wise, 14.9 wt%; volume-wise, 82 ~ 147 g/L) [6,7]. Regrettably, it releases hydrogen only at higher temperatures and lower rates, and gains partial reversible hydrogen absorption under harsh hydrogenation conditions [8]. Multiple measures including doping with catalysts or additives [6,9], preparing nanostructures [10], mixing with other metal hydrides or complex hydrides to form unstable systems [11,12], synthesizing derivatives such as ammonates of $Mg(BH_4)_2$ [13,14], have been taken to ameliorate these issues. Studies have revealed that the utilization of transition metal-based catalysts in $Mg(BH_4)_2$ could ameliorate its hydrogen storage properties, particularly the dehydriding kinetics [15].

* Corresponding author.
E-mail address: wuying@ncepu.edu.cn (Y. Wu).

https://doi.org/10.1016/j.cej.2023.147387
Received 18 September 2023; Received in revised form 4 November 2023; Accepted 13 November 2023
Available online 14 November 2023
1385-8947/© 2023 Elsevier B.V. All rights reserved.

Some excellent modifying effects exist in titanium-based and niobium-based catalysts [16–20]. According to the research by Bardají *et al.* [16], the addition of 5 mol% $NbCl_5$ or $TiCl_3$ to $Mg(BH_4)_2$ brought about a considerably lowered initiation temperature of dehydrogenation in the composites compared with that in pure $Mg(BH_4)_2$. At 300 °C, high amounts of hydrogen (5.5 and 6.3 wt%) could be released from the two composites, which were far more than that from $Mg(BH_4)_2$. However, the influencing mechanism of the additives on the dehydrogenation reaction was not clarified in detail. It was reported that NbF_5 resulted in outstanding dehydrogenation behavior in $Mg(BH_4)_2$, such as extremely low onset dehydriding temperature (~75 °C) and large H_2 yield at 150 ~ 300 °C (3.7 ~ 10.0 wt%) in the 15 wt% NbF_5-catalyzed sample) [17]. Additionally, Wang *et al.* [18] also declared the superior dehydrogenation properties and reversibility existing in the NbF_5-catalyzed Mg $(BH_4)_2$ composite. NbF_5 was proved to react with $Mg(BH_4)_2$, generating MgF_2 and NbB_2 during the dehydrogenation process, which were speculated to be a reason for the enhanced hydrogen storage performances. As clarified by Sulaiman *et al.* [19], the $2LiAlH_4 + Mg(BH_4)_2$ composite could be further destabilized by adding 5 wt% of TiF_3. Concretely, the TiF_3-catalyzed composite could release hydrogen from a decreased temperature at 60 °C, enhance the isothermal de/hydrogenation kinetics, and sharply lower the activation energies for the three main decomposition steps. According to the structural studies, Ti-Al, TiH_2, LiF, and MgF_2 formed as $2LiAlH_4 + Mg(BH_4)_2 + TiF_3$ decomposed, altering the de/hydrogenation pathways. As reported by Wang *et al.* [20], the optimizations of dehydriding kinetics and reversibility of Mg $(BH_4)_2$ were achieved through utilizing Ti nano-particles (NPs) which resulted from the generation of $TiH_{1.924}$, TiB, and TiB_2. These results manifested that Ti metal, TiX, and NbX (X = Cl, F) both showed modification effects on $Mg(BH_4)_2$ mainly through participating in its dehydrogenation reactions.

Recently, 2D transition metal carbides (MXenes), such as Ti_3C_2, Ti_2C, Nb_2C and V_2C, have been used as efficient catalysts in various hydrogen storage materials, including metal borohydrides [21,22], metal hydrides [23–27], and $NaAlH_4$ [28]. Zheng *et al.* [21] reported that the addition of 40 wt% Ti_3C_2 to $Mg(BH_4)_2$ resulted in a hydrogen release of 10.8 wt% at 330 °C within 15 min, as well as an improved kinetics in the dehydrogenation cycles. Based on investigations into the catalytic mechanism, Ti_3C_2 could prevent $Mg(BH_4)_2$ particles from agglomerating during cycling, and the *in-situ* formed Ti metal particles on the surfaces of Ti_3C_2 served as active catalysts, promoting the breakdown of B-H bonds during dehydrogenation. Other transition metal carbides, such as Ti_2C and Nb_2C, have been proven to result in excellent hydrogen storage performances in MgH_2 [23]. The MgH_2@Nb_2C and MgH_2@Ti_2C composites exhibited significantly reduced dehydrogenation apparent activation energies (111.49 kJ mol^{-1} and 86.48 kJ mol^{-1}) and higher capacity retention (95 % and 97 %) after 30 cycles [23]. The authors clarified that the unique layered structures in the MXenes and the valence state changes of the surficial multivalent transition metal atoms facilitated hydrogen transport and electron transfer in MgH_2. Based on these catalytic mechanisms, it is speculated that Ti_2C and Nb_2C MXenes should be capable of catalyzing the dehydrogenation of $Mg(BH_4)_2$, although there have been no relevant reports to date.

Herein, inspired by these studies, Ti_2C and Ti_3C_2 were synthesized through etching and utilized along with the commercially purchased Nb_2C MXene to catalyze the de/rehydrogenation performances of Mg $(BH_4)_2$. Isothermal and non-isothermal desorption measurements were exploited to comparatively assess the dehydrogenation properties of the $Mg(BH_4)_2$-30MXenes (Ti_3C_2, Ti_2C, Nb_2C). The enhanced dehydrogenation kinetics and increased H_2 contents are observed in all three Mg $(BH_4)_2$-30MXene composites, and the catalysis of Ti_2C triggers the optimum dehydrogenation properties. In the TPD (temperature-programmed desorption) test, the $Mg(BH_4)_2$-30Ti_2C composite liberates 13.2 wt% H_2 when heated to 500 °C with an initiation temperature of 132 °C. Besides, it yields 10.2 wt% H_2 at a relatively moderate temperature of 260 °C during the isothermal test. The structural evolutions of $Mg(BH_4)_2$ and MXenes during the TPD tests were analyzed. By means of theoretical calculations and structural characterizations, the catalyzing effects of the MXenes are confirmed to stem from multiple factors. Furthermore, the improved reversibility of $Mg(BH_4)_2$-30MXenes as well as the products of $Mg(BH_4)_2$-30Ti_2C during the cycles was also discussed.

2. Experimental methods

2.1. Materials and chemicals

Magnesium chloride ($MgCl_2$, 99 %), sodium borohydride ($NaBH_4$, 98 %), and lithium fluoride (LiF, 99.99 %) were purchased from Aladdin. Powders of titanium aluminum carbide (Ti_3AlC_2) and multi-layered niobium carbide (Nb_2C) were provided by 11 Technology, Co., Ltd. Ti_2AlC powder was bought from Foshan Xinxi Technology Co., Ltd. Hydrochloric acid (36 %~38 %) and diethyl ether (AR) were acquired from Sinopharm Chemical Reagent, Co., Ltd. Prior to use, diethyl ether was dried overnight with calcium hydride (CaH_2). Furthermore, the remaining chemicals were employed in their original state without any additional treatment.

2.1.1. Synthesis of $Mg(BH_4)_2$

$Mg(BH_4)_2$ was synthesized using a previously described method [29], which was based on the reaction outlined below.

$$2NaBH_4 + MgCl_2 \rightarrow Mg(BH_4)_2 + 2NaCl \quad (1)$$

Under an argon atmosphere, $NaBH_4$ and $MgCl_2$ were ball-milled utilizing a planetary ball mill (Frisch Pulverisette-6) with a molar ratio of 2:1. The ratio of weight between the balls and powder was 120 to 1, and the milling process continued for a total time of 18 h at a rotational speed of 500 revolutions per minute (rpm). The milling stopped for 6 min every 12 min and then continued in the opposite rotation direction. Following the initial milling process, an ample amount of dehydrated diethyl ether was introduced into the stainless steel pot. To guarantee complete desolvation of the produced $Mg(BH_4)_2$ in diethyl ether, the mixture underwent an additional 24-hour wet milling at a speed of 300 rpm. After filtering, the solution of $Mg(BH_4)_2$ was separated from the insoluble NaCl, and was subsequently heated at 200 °C under a dynamic vacuum for 24 h to obtain a pure powder of $Mg(BH_4)_2$. The preparation process was under an air-free environment, and the obtained $Mg(BH_4)_2$ was stored in a glovebox (Mikrouna Super 1220/750/900, Mikrouna (Shanghai) Ind. Int. Tech. Co., Ltd.) full of argon, with concentrations of O_2 and $H_2O < 0.01$ ppm.

2.1.2. Synthesis of Ti_3C_2 and Ti_2C MXenes

Initially, 0.5 g of lithium fluoride was mixed with 10 mL of 9 M hydrochloric. Subsequently, the mixture was stirred for 40 min and gradually added with 0.5 of Ti_3AlC_2 powder. Next, the etching process was continued for 24 h with continuous stirring at 35 °C. The resulting solid mixture was then separated from the solution through centrifugation and rinsed multiple times with deionized water to ensure the pH level above 6. About 5–10 min sonication and handshaking were conducted during each wash to assist in the removal of impurities. Afterward, the near-neutral turbid liquid containing Ti_3C_2 was subjected to a ten-minute centrifugation at 800 rpm and the upper suspension was collected. The pure Ti_3C_2 MXene was ultimately obtained after vacuum freeze-drying of the suspension. To synthesize Ti_2C, 0.6 g of Ti_2AlC powder was added slowly to the etchant of LiF (0.5 g)/ HCl (15 mL, 9 M) and etched with a 48-hour stir. The subsequent washing, extracting, and drying procedures were identical to those of Ti_3C_2.

2.1.3. Preparation of the $Mg(BH_4)_2$-MXene composites

Before use, the freeze-dried Ti_3C_2, Ti_2C, and the as-received Nb_2C powders were heated at 105 °C with vacuumizing for 12 h to further

remove H_2O. $Mg(BH_4)_2$ doped with 30 wt% MXene (Ti_3C_2, Ti_2C, Nb_2C) (donated as $Mg(BH_4)_2$-30Ti_3C_2, $Mg(BH_4)_2$-30Ti_2C, $Mg(BH_4)_2$-30Nb_2C throughout the text) were prepared. A mixture of 90 mg of MXene and 210 mg of $Mg(BH_4)_2$ was milled for 10 h at 500 rpm with a 120:1 ball-to-powder ratio. The $Mg(BH_4)_2$-$x$$Ti_2C$ (x = 10, 20, 40 wt%) composites as well as the as-milled $Mg(BH_4)_2$ were obtained under the same processing conditions.

2.2. Material characterizations

X-ray diffraction (XRD) tests on a Bruker D8 Advance instrument were conducted to analyze the crystal structures, in which Cu Kα (1.542 Å) radiation was employed. The samples were sealed with tape in a glovebox before the test to insulate them from the air. Fourier transform infrared spectroscopy (FTIR) analyses were performed on a Bruker Vertex 70 spectrometer to detect the bond characteristics. Each powder sample was fully dispersed in dried KBr with a 1:200 weight ratio, and the mixture was pressed into a transparent pellet in the glovebox for each measurement. Scanning electron microscope (SEM) pictures and energy dispersive X-ray spectroscopy (EDS) elemental mappings were acquired on an FEI Nova NanoSEM 450 to observe the morphologies. X-ray photoelectron spectroscopy (XPS) spectra were acquired on a Thermo Fisher Nexsa with a monochromatic Al Kα (1486.6 eV) X-ray source to examine the chemical valence states of Ti, Nb, Mg, B, and F. The XPS primary data of all the elements were calibrated before fitting according to the binding energy of C1s (284.8 eV).

2.3. Hydrogen storage property measurements

The dehydrogenation measurements for the $Mg(BH_4)_2$-MXene composites as well as pure $Mg(BH_4)_2$ based on the Sieverts method were performed on a homemade HPSA-auto apparatus, which had been carefully calibrated. About 30 mg of the specimen was sealed within a stainless steel tubular reactor with a known volume in a glovebox. After being connected to the instrument, the pressure and the temperature inside the reactor were monitored and recorded in real-time. These collected data were employed to calculate the amount of hydrogen released using the ideal gas state equation. The H_2 desorption capacity in this work was calculated according to the content of $Mg(BH_4)_2$ in each composite. Under an initial pressure of $< 1 \times 10^{-4}$ bar, temperature-programmed desorption (TPD) tests were performed by heating the samples to 500 °C at 5 °C min^{-1}. Isothermal dehydrogenation tests were conducted by rapidly heating the samples to a certain preset temperature (240, 260, 280 and 300 °C) and holding them for 6 h. The isothermal dehydrogenation data were adopted to calculate the dehydrogenation apparent activation energy (E_a) of each sample based on the Arrhenius equation [30] as follows.

$$\mathrm{rate(wt\%/h)} = k_0 \exp(-E_a/RT) \quad (2)$$

Where k_0 is a constant, R is the gas constant (8.314 J mol^{-1} K^{-1}), and T is temperature (in Kelvin).

After the isothermal dehydrogenation tests at 260 °C, the products underwent hydrogenation at 300 °C under 100 bar H_2 pressure for 8 h. Subsequently, the dehydrogenation cycle performance was determined by the second and third isothermal dehydrogenation at 260 °C.

2.4. Computational methods

To investigate the dehydrogenation of $Mg(BH_4)_2$ influenced by Ti_3C_2, Ti_2C, and Nb_2C, density functional theory (DFT) calculations were conducted with the Vienna ab initio simulation package (VASP 5.3.5, Vienna, Austria) [31]. The interaction between electrons and ions was depicted utilizing the projector augmented wave pseudopotential [32], while the exchange–correlation energy of interacting electrons was treated using the Perdew-Burke-Ernzerhof generalized gradient approximation [33]. The plane wave basis energy cut-off was set to 500 eV. The geometry optimization of the $Mg(BH_4)_2$ molecule involved placing it into a 10 × 10 × 10 Å box, with a relaxation process completed employing a 3 × 3 × 3 Monkhorst-Pack k-point grid, the optimized result is shown in Fig. S12 (Supporting Information). The geometry optimization of MXene and $Mg(BH_4)_2$-MXene was performed employing a 2 × 2 × 1 Monkhorst-Pack k-point grid, while electronic structure calculations were executed on a significantly denser k-point grid. To simulate the surfaces of Ti_3C_2, Ti_2C, and Nb_2C, slab models were constructed with a surface period of (4 × 4) and separated by more than 15 Å of vacuum. All structures considered were fully optimized, ensuring a force of < 0.01 eV/Å on per atom. The atomic charge was computed using the Bader analysis algorithm [34]. The adsorption energies of $Mg(BH_4)_2$ molecule on different MXenes were calculated according to the following formula.

$$E_{adsorption} = E_{total} - E_{surface} - E_{molecule} \quad (3)$$

where $E_{molecule}$ and $E_{surface}$ are the energies of $Mg(BH_4)_2$ molecule and the MXene surface, respectively. E_{total} is the total energy of the system that $Mg(BH_4)_2$ molecule adsorbed on the MXene surface.

3. Results and discussion

The two-dimensional morphologies, as depicted in Fig. 1a-c, of the as-synthesized Ti_3C_2, Ti_2C, and the commercial Nb_2C MXene are evidenced using scanning electron microscope (SEM). From Fig. 1a, the obtained Ti_3C_2 is observed to exhibit a few-layered sheet structure. The Al layer being etched away, and the in-situ generated LiCl by the reaction of HCl with LiF acting as an intercalator [35] contribute to the Ti_3C_2 sheets easily being delaminated in the washing process. Unlike the Ti_3C_2 MXene, the Ti_2C and Nb_2C MXenes exhibit multi-layered accordion-like structures (Fig. 1b-c).

The crystal structures of the Ti_3C_2, Ti_2C, Nb_2C, and their corresponding MAX powders were characterized by employing X-ray diffraction (XRD) (Fig. 1d-f). As given in Fig. 1d, the (0 0 2) peak of Ti_3AlC_2 located at $2\theta = 9.5°$ downshifts to 6.9° after exfoliation, and no MAX phase is detected in the etched product, indicating the complete conversion into Ti_3C_2 MXene [36]. A similar phenomenon could be observed when comparing the XRD data of Ti_2AlC and the as-prepared Ti_2C. When the Ti_2AlC MAX is etched, the (0 0 2) characteristic peak also shifts from 13.0° toward a lower angle (7.8°) (Fig. 1e), implying the successful formation of Ti_2C MXene [37]. The peaks of Ti_2AlC disappear except for the extremely weak peak at 39.2° in the XRD pattern of Ti_2C, suggesting that the vast majority of the Al layer has been extracted. The sufficient etchings for Ti_3C_2 and Ti_2C MXenes are further confirmed by the XPS analyses as no obvious peaks related to the Al element are detected (Fig. S1, Supporting Information). The (0 0 2) peak of Nb_2AlC appears at $2\theta = 12.7°$, while that of Nb_2C downshifts to 7.4° (Fig. 1f), meaning that its interlayer spacing has been enlarged after the removal of the Al layer. Nevertheless, the presence of some residual Nb_2AlC and NbC impurities [38,39] are also detected in the as-received Nb_2C MXene. The XPS survey spectra of the three MXenes (Fig. S1, Supporting Information) show that besides the corresponding transition metals and C element, O, F, and Cl are detected in Ti_3C_2 and Ti_2C, while O and F elements are detected in Nb_2C. This represents a difference in functional groups on the surfaces of the MXenes, which is attributed to the utilization of different etchants (Ti_3C_2 and Ti_2C: LiF + excess HCl; Nb_2C: HF).

With the ball milling treatment, the $Mg(BH_4)_2$-30MXene (Ti_3C_2, Ti_2C, Nb_2C) composites were prepared. The structures and bond vibrations of the three composites as well as the as-milled $Mg(BH_4)_2$ were studied at room temperature (RT) using XRD and FTIR (Fourier transform infrared spectroscope) techniques (Fig. 2a-b). The XRD data (Fig. S2, Supporting Information) of the $Mg(BH_4)_2$ obtained *via* wet chemical synthesis in this work agrees well with that of orthorhombic $Mg(BH_4)_2$ (β-phase) [40]. No diffraction peaks of $NaBH_4$, $MgCl_2$, and

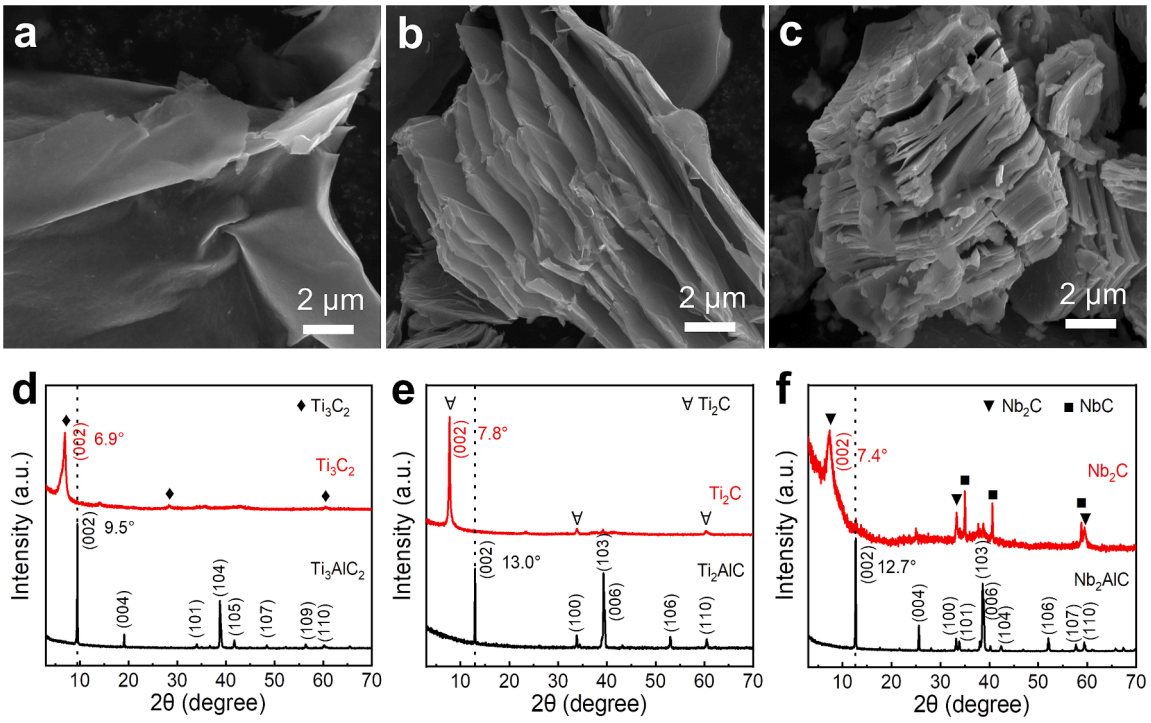

Fig. 1. SEM images of (a) Ti_3C_2, (b) Ti_2C, and (c) Nb_2C. XRD patterns of (d) Ti_3AlC_2 (PDF # 52–0875) and Ti_3C_2, (e) Ti_2AlC (PDF # 29–0095) and Ti_2C, (f) Nb_2AlC (PDF # 30–0033) and Nb_2C.

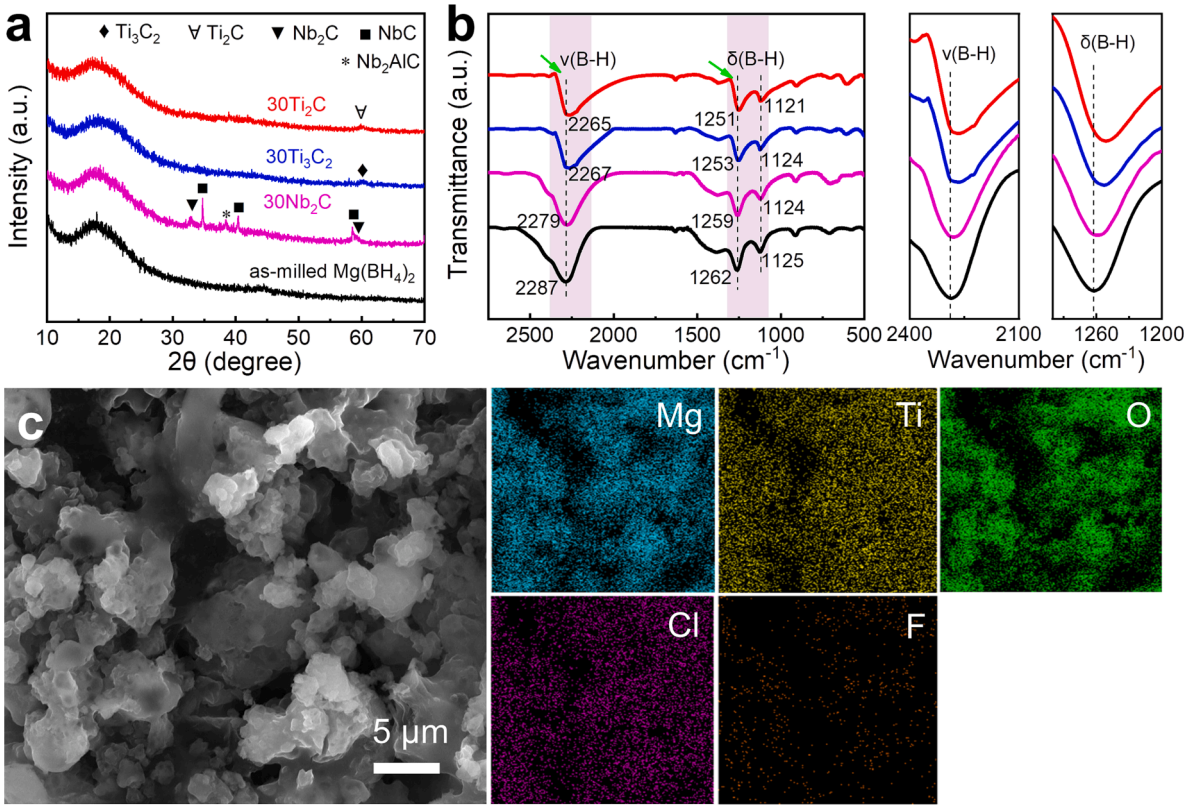

Fig. 2. (a) XRD patterns and (b) FTIR spectra of the as-milled $Mg(BH_4)_2$ and $Mg(BH_4)_2$-30MXene (Ti_3C_2, Ti_2C, Nb_2C) composites. (c) SEM image and EDS mapping results of the as-milled $Mg(BH_4)_2$-30Ti_2C composite.

NaCl are detected, representing the obtainment of pure $Mg(BH_4)_2$. However, for the ball-milled $Mg(BH_4)_2$, the XRD pattern presents no sharp peaks except for a diffuse scattering peak at 15°~25° (2θ) belonging to the amorphous tape (Fig. 2a). This suggested that the ball milling treatment brings about amorphization of $Mg(BH_4)_2$, aligning with the finding presented by Li *et al.* [41] The as-milled $Mg(BH_4)_2$-

30MXene (Ti_3C_2, Ti_2C, Nb_2C) composites exhibit only a few weak characteristic peaks in the XRD patterns, corresponding to the crystalline Ti_3C_2, Ti_2C, and Nb_2C with the original impurities therein, respectively. Fig. 2b displays the FTIR spectra of the as-milled $Mg(BH_4)_2$-MXene composites as well as pure $Mg(BH_4)_2$. One broad absorption band at 2287 cm^{-1} and two absorption bands at 1262 cm^{-1}, 1125 cm^{-1} could be seen from the FTIR spectrum of $Mg(BH_4)_2$, which represents the stretching and bending vibrations of B-H bonds in the $[BH_4]^-$ groups [42]. The $Mg(BH_4)_2$-MXene composites are observed to display similar FTIR spectra to that of $Mg(BH_4)_2$. However, their B-H vibration bands are detected to shift towards lower wavenumber (red-shift), *e.g.*, from 2287 cm^{-1} and 1262 cm^{-1} for $Mg(BH_4)_2$ to 2265 cm^{-1} and 1251 cm^{-1} for the $Mg(BH_4)_2$-30Ti_2C composite, evidencing that the strengths of the B-H bonds have been weakened [43,44]. The red-shift extent in the Mg $(BH_4)_2$-30Ti_2C composite is the largest, followed by $Mg(BH_4)_2$-30Ti_3C_2, and that in $Mg(BH_4)_2$-30Nb_2C is the smallest. This result indicates an interaction existing between $Mg(BH_4)_2$ and each MXene that could decrease the stability of B-H bonds, and notably Ti_2C MXene shows the strongest interaction with $Mg(BH_4)_2$ in this regard. In addition, the micromorphology of the $Mg(BH_4)_2$-30Ti_2C composite is observed by SEM as an example (Fig. 2c). From its SEM image, the layered and even lamellar MXene is found to exist among the particles below several microns in size. The energy dispersive X-ray spectroscopy (EDS, Fig. S3, Supporting Information) spectrum displays strong signals from Mg, Ti, C, O and Cl, as well as weak signals from B and F elements, confirming the coexistence of $Mg(BH_4)_2$ and Ti_2C. The EDS elemental mapping results further prove the uniform distribution of the Mg, Ti, O, Cl and F elements throughout the composite, which indicates the full contact of $Mg(BH_4)_2$ with Ti_2C.

Temperature-programmed desorption (TPD) and isothermal dehydrogenation measurements were conducted to manifest the effects of MXenes in boosting the dehydrogenation kinetics performance of Mg $(BH_4)_2$. Firstly, for the purpose of finding out the optimal additive amount that could result in the most enhanced hydrogen desorption behavior, $Mg(BH_4)_2$ doped with various amounts of Ti_2C (10, 20, 30 and 40 wt%), as an example, were subjected to the dehydrogenation tests. Besides, the TPD and isothermal dehydrogenation curve of pure Mg $(BH_4)_2$ were also tested for comparison. As illustrated in the TPD curves and the corresponding derivative curves (Figs. S4-S5, Supporting Information), all the $Mg(BH_4)_2$-$x$$Ti_2C$ (x = 10, 20, 30 and 40 wt%) composites show significantly decreased onset (148, 144, 132 and 110 °C) and peak (295, 288, 281 and 252 °C) dehydrogenation temperatures compared to those of $Mg(BH_4)_2$ (275 °C, 359 °C). Thus increasing the Ti_2C amount could facilitate the decomposition of $Mg(BH_4)_2$ at a lower temperature. However, introducing Ti_2C also affects the released H_2 content. It should be noted that the H_2 desorption capacity in this work is calculated according to the content of $Mg(BH_4)_2$ in each composite. As depicted in Fig. S4 (Supporting Information), the H_2 desorption capacities (considering only $Mg(BH_4)_2$) of the $Mg(BH_4)_2$-$x$$Ti_2C$ composites improve to 12.2, 12.6 and 13.2 wt% ($Mg(BH_4)_2$: 11.9 wt%) at 500 °C when 10, 20 and 30 wt% Ti_2C are added, respectively. However, it decreases to 11.6 wt% H_2 when the Ti_2C content further increases to 40 wt %. This is mainly due to that part of $Mg(BH_4)_2$ undergoes reactions with Ti_2C MXene and its abundant groups such as Cl and F during milling, resulting in partial loss of H_2 capacity [45]. Furthermore, according to the isothermal dehydrogenation results of the four composites (Fig. S6, Supporting Information), the highest H_2 desorption capacity reaching 10.2 wt% is observed in the $Mg(BH_4)_2$-30Ti_2C composite within 360 min

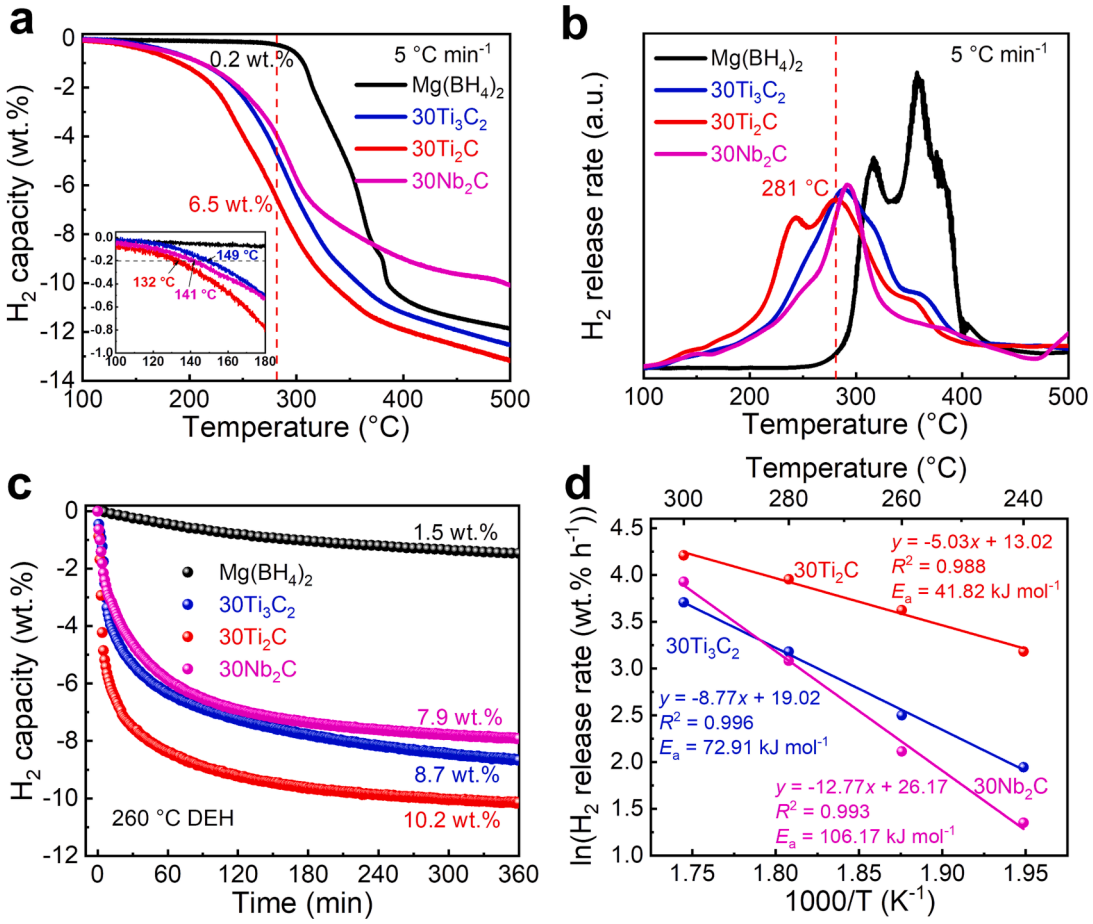

Fig. 3. (a) TPD curves, (b) TPD derivative curves, (c) isothermal dehydrogenation curves at 260 °C, and (d) the Arrhenius plots of the as-milled $Mg(BH_4)_2$-30MXene (Ti_3C_2, Ti_2C, Nb_2C) composites.

at 260 °C. Therefore, 30 wt% is thought to be the optimal additive amount of Ti_2C when considering both the dehydrogenation temperature and H_2 capacity.

Next, the dehydrogenation properties of $Mg(BH_4)_2$ doped with 30 wt % of different MXenes (Ti_3C_2, Ti_2C, Nb_2C) are investigated. From the TPD results (Fig. 3a) and their derivative curves (Fig. 3b), the $Mg(BH_4)_2$-30Ti_2C composite shows lower onset and peak dehydrogenation temperatures (132 °C, 281 °C) than those of the $Mg(BH_4)_2$-30Ti_3C_2 (149 °C, 289 °C) and $Mg(BH_4)_2$-30Nb_2C (141 °C, 293 °C) composites. Nonetheless, the H_2 release temperatures of all the composites exhibit a significant decrease in comparison with that of $Mg(BH_4)_2$, indicating that Ti_3C_2, Ti_2C, and Nb_2C all could well catalyze the dehydrogenation of $Mg(BH_4)_2$. When heated to 281 °C, the $Mg(BH_4)_2$-30MXenes (Ti_3C_2, Ti_2C, Nb_2C) composites liberates 4.7, 6.5 and 3.9 wt% H_2, respectively, while pure $Mg(BH_4)_2$ releases only 0.2 wt% H_2. The hydrogen yield of the $Mg(BH_4)_2$-30Ti_3C_2 composite at 500 °C is 12.5 wt%, 0.7 wt% lower than that of $Mg(BH_4)_2$-30Ti_2C. Whereas the $Mg(BH_4)_2$-30Nb_2C composite liberates 10.1 wt% H_2 (~500 °C), which is even lower than 11.9 wt% of $Mg(BH_4)_2$. It could be caused by the too many F groups on the Nb_2C surfaces derived from the etching agent (concentrated HF solution), which consumed a certain amount of $Mg(BH_4)_2$ during milling. From the isothermal dehydrogenation results at 260 °C (Fig. 3c), the hydrogen yield of $Mg(BH_4)_2$-30Ti_2C (10.2 wt%) within 360 min is 1.5 wt% larger than that of $Mg(BH_4)_2$-30Ti_3C_2, and 2.3 wt% larger than that of Mg

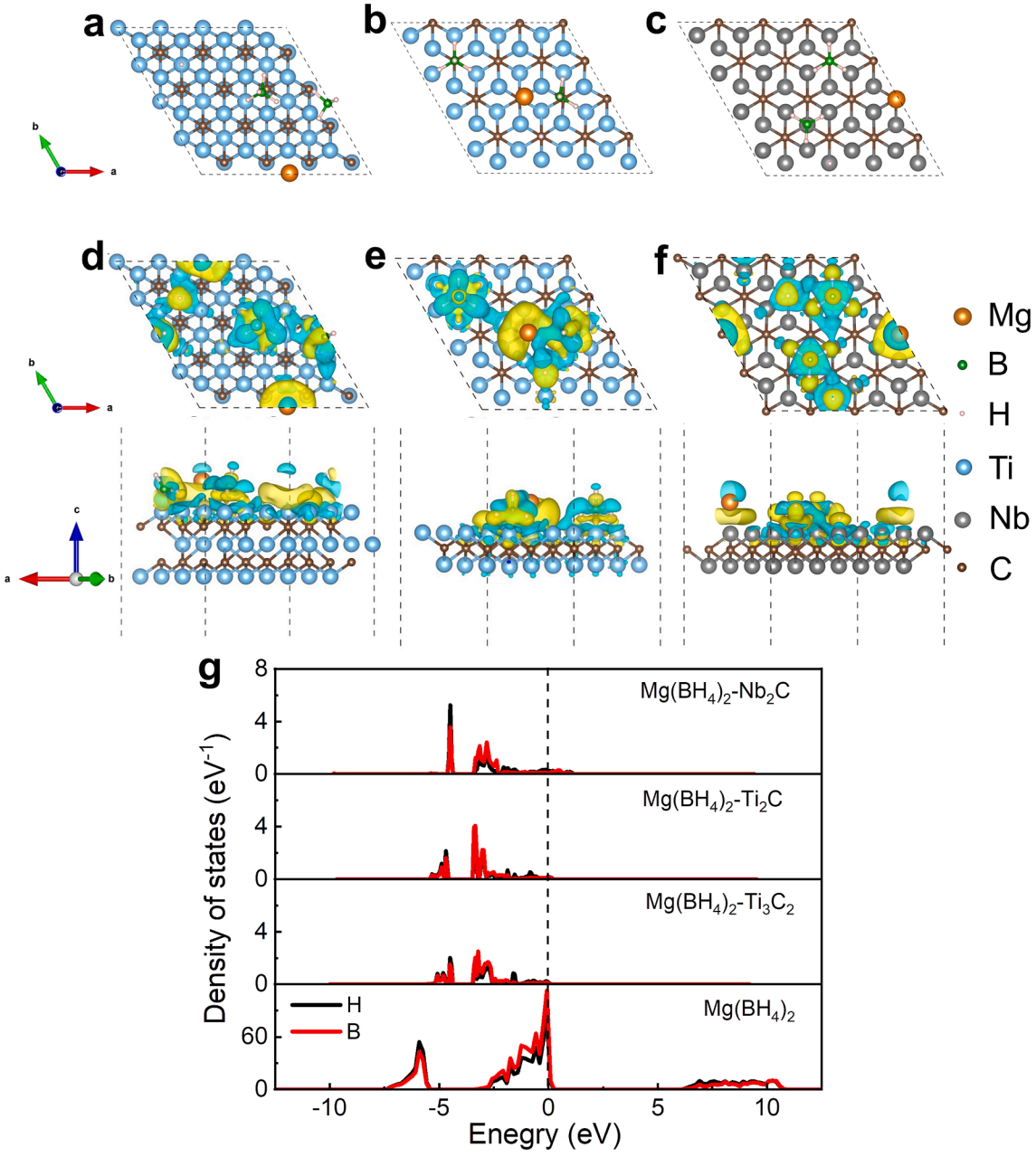

Fig. 4. DFT calculation of the $Mg(BH_4)_2$/MXene interfaces. Optimized adsorption structures of the $Mg(BH_4)_2$ molecule on the surfaces of (a) Ti_3C_2, (b) Ti_2C, and (c) Nb_2C. Difference charge density (top views and side views) for (d) $Mg(BH_4)_2$-Ti_3C_2, (e) $Mg(BH_4)_2$-Ti_2C, and (f) $Mg(BH_4)_2$-Nb_2C. The yellow and blue regions indicate space charge accumulation and depletion, respectively. (g) Density of states (DOS) for $Mg(BH_4)_2$-MXenes (Ti_3C_2, Ti_2C, Nb_2C) and pure $Mg(BH_4)_2$, the dashed line shows the position of the Fermi energy level. (For interpretation of the references to colour in this figure legend, the reader is referred to the web version of this article.)

$(BH_4)_2$-30Nb_2C. The actual H_2 desorption capacities of $Mg(BH_4)_2$-30MXenes (Ti_2C, Ti_3C_2, Nb_2C) are 7.1, 6.1 and 5.5 wt% respectively, even so, which are much larger than 1.5 wt% H_2 of $Mg(BH_4)_2$.

To quantitatively evaluate the improved dehydriding kinetics of the $Mg(BH_4)_2$-30MXenes (Ti_2C, Ti_3C_2, Nb_2C), their dehydrogenation apparent activation energies (E_a) are further calculated using the Arrhenius formula based on their isothermal dehydrogenation curves at various temperatures (240, 260, 280 and 300 °C) (Figs. S7-S9, Supporting Information). Through linear fitting analysis of the Arrhenius plots (Fig. 4d), the dehydrogenation activation energies are obtained to be 41.82 kJ mol^{-1} for $Mg(BH_4)_2$-30Ti_2C, 72.91 kJ mol^{-1} for $Mg(BH_4)_2$-30Ti_3C_2, and 106.17 kJ mol^{-1} for $Mg(BH_4)_2$-30Nb_2C, which are all remarkably lower than the E_a (166.86 kJ mol^{-1}) value of pure $Mg(BH_4)_2$ as calculated in Fig. S10 (Supporting Information). Therefore, the introductions of the MXenes contribute to reducing the kinetic barrier for H_2 desorption from $Mg(BH_4)_2$. Based on the above results, the Mg $(BH_4)_2$-30Ti_2C composite exhibits the most enhanced dehydriding kinetics performance and the highest H_2 capacity, suggesting that Ti_2C MXene is the optimal catalyst among the three MXenes for the hydrogen desorption of $Mg(BH_4)_2$.

Density functional theory (DFT) calculations were conducted to investigate the effects of Ti_3C_2, Ti_2C, and Nb_2C MXenes, respectively on the dehydrogenation of $Mg(BH_4)_2$. The three MXene surfaces were modeled using slabs with (4 × 4) unit cells (Fig. S11, Supporting Information). For each surface, three sites were tested to determine the optimal adsorption site, from which the adsorption structure of Mg $(BH_4)_2$ molecule on each MXene surface was constructed, as shown in Fig. S13 (Supporting Information). And the optimized adsorption structures (Fig. 4a-c) were used to model the dehydrogenation reactions in the $Mg(BH_4)_2$-MXene systems. Through the DFT calculations, the adsorption energies of $Mg(BH_4)_2$ molecule on the MXenes, the changed B-H bond lengths, the interfacial charge density difference, the atomic charge, and the density of states (DOS) were analyzed (Fig. 4d-g; Table S1, Supporting Information). The models are built with the following considerations: i) $Mg(BH_4)_2$ crystal is composed of $Mg(BH_4)_2$ molecules; ii) the dehydrogenation of $Mg(BH_4)_2$ results from the breakdown of B-H bonds.

For all the three $Mg(BH_4)_2$-MXene adsorption structures in Fig. 4a-c, the $[BH_4]^-$ group appears to escape from the pull of the Mg atom and be adsorbed on the MXene, suggesting that all three MXenes could weaken the ionic bond between $[BH_4]^-$ and Mg. As listed in Table S1 (Supporting Information), the adsorption energies of the $Mg(BH_4)_2$ molecule on Ti_3C_2, Ti_2C, and Nb_2C are calculated to be −6.07649, −6.34232 and −7.24207 eV respectively, indicating the successful adsorption of Mg $(BH_4)_2$ molecule on each surface. The adsorption energy of $Mg(BH_4)_2$ on Nb_2C is the highest (absolute value). Thus, two H atoms break away from $[BH_4]^-$ and are adsorbed on Nb_2C, while only one H atom off $[BH_4]^-$ is adsorbed on Ti_3C_2 or Ti_2C. $Mg(BH_4)_2$ on Ti_2C shows moderate adsorption energy, which not only ensures the adsorption reaction but also is convenient for the H escaping from the surface during the later dehydrogenation process. After adsorption, compared with the B-H bonds in the $Mg(BH_4)_2$ crystal, those in the $Mg(BH_4)_2$ molecule away from the interfaces are slightly shortened, while the other ones are stretched to varying degrees. The extent for the stretch of B-H bonds is the greatest in $Mg(BH_4)_2$-Ti_2C, the second greatest in $Mg(BH_4)_2$-Ti_3C_2, and the smallest in $Mg(BH_4)_2$-Nb_2C. Therefore, all the MXenes could weaken the B-H bonds in $Mg(BH_4)_2$, and Ti_2C shows the best effect. The obtained result aligns with the previous analysis result of FTIR as shown in Fig. 2b.

The difference charge density distributions of the $Mg(BH_4)_2$-MXenes are depicted in Fig. 4d-f. It is observed that on all the interfaces, MXene interacts electronically with $[BH_4]^-$, providing a large number of electrons to $[BH_4]^-$. The H atoms gain electrons, while the B atoms lose electrons. It is this interfacial charge transfer that contributes to weakening the B-H bonds in $[BH_4]^-$. The corresponding electron transfer amount obtained by Bader charge analysis is summarized in Table S1 (Supporting Information). The total charge gain amount of the H atoms in each adsorption structure is in the following order: $Mg(BH_4)_2$-Ti_2C > $Mg(BH_4)_2$-Ti_3C_2 > $Mg(BH_4)_2$-Nb_2C. Additionally, the central Mg atom undergoes a strong electronic interaction with the MXene, resulting in the weakening of the ionic bond between Mg^{2+} and $[BH_4]^-$. The DOS (Fig. 4g) shows that the occupations of B-2p and H-1s orbitals in the Mg $(BH_4)_2$-MXenes are significantly decreased and exhibit a discrete character compared with that in $Mg(BH_4)_2$. This implies a significantly weakened hybridization between B and H orbitals in the $Mg(BH_4)_2$-MXenes, which is another reason for the weakening of the B-H bonds [46]. The DFT calculation results bring a deep understanding of the Mg $(BH_4)_2$-MXene (Ti_3C_2, Ti_2C, Nb_2C) interfaces and the catalytic mechanisms of the MXenes for the dehydrogenation of $Mg(BH_4)_2$.

To investigate the dehydrogenation mechanism of the MXenes-involved $Mg(BH_4)_2$, a series of structural characterizations were conducted, including XRD, FTIR, and XPS analyses. The XRD patterns (Fig. 5) and FTIR spectra (Fig. S14, Supporting Information) of the dehydrogenated $Mg(BH_4)_2$-30MXene (Ti_3C_2, Ti_2C, Nb_2C) composites after the TPD tests (RT ~ 500 °C) are measured. All the dehydrogenated $Mg(BH_4)_2$-30MXenes exhibit poor crystallinity, and several weak peaks from MgB_2 ($2\theta = 33.5°$, 42.4°; PDF # 38–1369) and the related MXene are detected from each XRD pattern in Fig. 5. As shown in Fig. S14 (Supporting Information), the IR absorbance peaks of B-H bonds disappear in the dehydrogenated $Mg(BH_4)_2$-30Ti_2C, while the peak of Mg-H bonds in MgH_2 at 500–750 cm^{-1} [47] is visible, indicating an incomplete dehydrogenation process. For the dehydrogenated Mg $(BH_4)_2$-30Ti_3C_2, the FTIR spectrum presents some weak B-H vibrations (stretching: 2293 and 2222 cm^{-1}, bending: 1125 cm^{-1}) of $Mg(BH_4)_2$, and stronger MgH_2 absorption peak compared with that in the dehydrogenated $Mg(BH_4)_2$-30Ti_2C, which is related to the lower H_2 release amount of $Mg(BH_4)_2$-30Ti_3C_2 during TPD test. As to the dehydrogenation products of $Mg(BH_4)_2$-30Nb_2C, besides the MgH_2 peak, a broad absorption around 2465 cm^{-1} and several distinct peaks in the region of 808–1444 cm^{-1} are observed, which are possibly due to the existence of residual $Mg(BH_4)_2$ and some polyborane intermediates such as $MgB_{12}H_{12}$ [48]. The FTIR result reveals a low extent of dehydrogenation reaction in $Mg(BH_4)_2$-30Nb_2C, which results in the lowest dehydrogenation content among the three $Mg(BH_4)_2$-30MXene composites.

XPS was used to analyze the chemical state of Ti and Nb elements in the as-prepared and dehydrogenated $Mg(BH_4)_2$-30MXenes (Fig. 5b-d). For comparison, the XPS spectra of Ti 2p in Ti_3C_2 and Ti_2C MXenes, and that of Nb 3d in Nb_2C MXene are also displayed. It is worth noting that the chemical state of Ti in Ti_3C_2 and Ti_2C MXenes is complicated owing to the oxygen-containing groups distributing on the surfaces [49,50]. For instance, considering the spin–orbit splitting [51], the Ti $2p_{3/2}$/$2p_{1/2}$ double peaks of Ti-C, Ti^{2+}, Ti^{3+}, and Ti^{4+}, centered at 454.9/460.9, 455.8/461.3, 457.1/462.7 and 459.0/464.7 eV, respectively, could be seen through fitting the XPS spectrum of Ti_2C (Fig. 5c). However, after milling with $Mg(BH_4)_2$, the intensities of Ti^{4+} and Ti^{3+} peaks are found to sharply decrease, and zero-valent titanium (Ti^0 $2p_{3/2}$/$2p_{1/2}$: 453.9/460.1 eV) appears due to the reducibility of $Mg(BH_4)_2$. After the TPD test, the Ti^{4+}, Ti^{3+}, and Ti^{2+} are further reduced to metallic Ti as the XPS spectrum of the dehydrogenated $Mg(BH_4)_2$-30Ti_2C presents. Similarly, the reduction of Ti with higher valences (Ti^{4+}, Ti^{3+}, and Ti^{2+}) to Ti^0 is also observed in the as-milled $Mg(BH_4)_2$-30Ti_3C_2 composite and its dehydrogenation products (Fig. 5b). The XPS Nb 3d spectrum of the Nb_2C MXene (Fig. 5d) is fitted with three components including Nb-C, Nb^{4+}, and Nb^{5+}, the Nb $3d_{5/2}$/$3d_{3/2}$ peaks of which are located at 203.7/206.4, 206.6/209.3, and 207.3/210.0 eV, respectively [52]. Part of Nb^{5+} is reduced to Nb^0 (202.9/205.7 eV) in the as-milled $Mg(BH_4)_2$-30Nb_2C. After dehydrogenation, the peaks related to Nb^{5+} and Nb^{4+} are greatly weakened and those of Nb^0 dominate the XPS spectrum. Thus, the reaction between $Mg(BH_4)_2$ and the high-valence Ti or Nb ions in the MXenes occurs during both the ball milling and heating stages, resulting in a gradual increase in the *in-situ* generated Ti^0 or Nb^0, which is distributed on the surfaces of the MXenes. However, there is no obvious

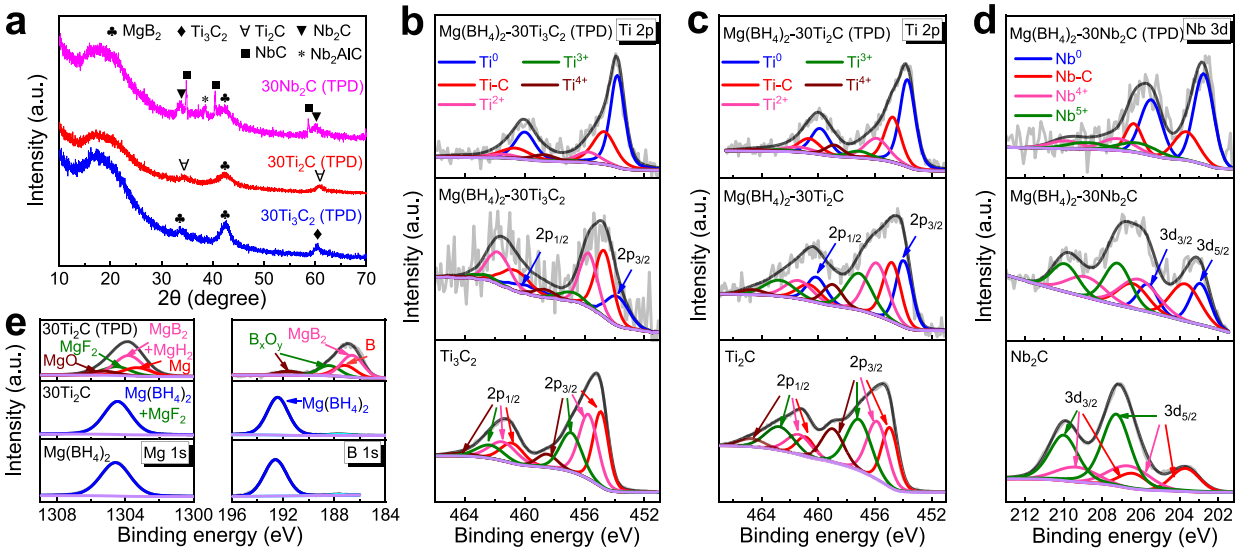

Fig. 5. (a) XRD patterns of the dehydrogenated $Mg(BH_4)_2$-30MXene (Ti_3C_2, Ti_2C, Nb_2C) composites at 500 °C. (b)-(c) High-resolution XPS profiles of Ti 2p and (d) Nb 3d in the MXenes, $Mg(BH_4)_2$-30MXenes, and their dehydrogenated productions after the TPD tests. (e) High-resolution XPS profiles of Mg 1 s and B 1 s in the as-prepared $Mg(BH_4)_2$, $Mg(BH_4)_2$-30Ti_2C, and its dehydrogenated productions after the TPD test.

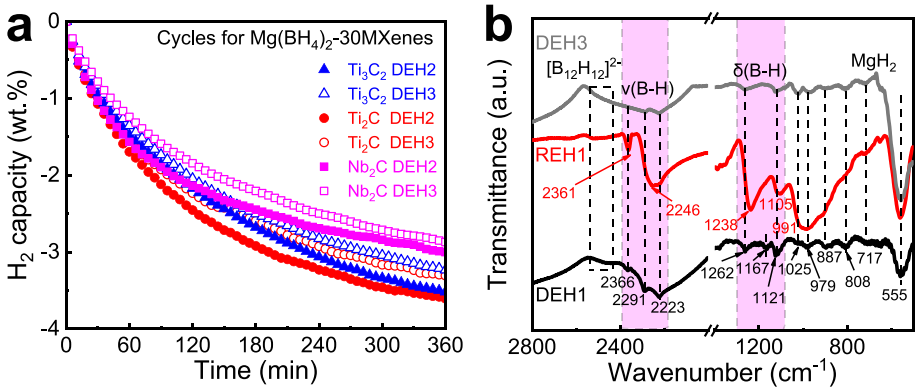

Fig. 6. (a) Isothermal cyclic dehydrogenation curves of the $Mg(BH_4)_2$-30MXene (Ti_3C_2, Ti_2C, Nb_2C) composites at 260 °C. (b) FTIR spectra of the 1st and 3rd dehydrogenated $Mg(BH_4)_2$-30Ti_2C composite at 260 °C and the 1st rehydrogenated $Mg(BH_4)_2$-30Ti_2C composite at 300 °C under 10 MPa H_2 pressure.

change in the Ti-C or Nb-C peaks in the $Mg(BH_4)_2$-30MXenes at different stages, indicating the structural stability of each MXene.

Taking the $Mg(BH_4)_2$-30Ti_2C composite as a representative, the Mg and B-containing phases in the dehydrogenation products were further investigated by XPS. As Fig. 5e shows, the peaks of Mg 1s and B 1s in the as-prepared $Mg(BH_4)_2$ are located at 1304.6 eV and 192.6 eV, respectively, while a very faint peak in the XPS B 1s spectrum around 187.7 eV is assumed to be an undetermined impurity. Combining the XPS results of Mg 1s, B 1s and F 1s in the $Mg(BH_4)_2$-30Ti_2C composite (Fig. 5e; Fig. S15, Supporting Information), a small amount of $Mg(BH_4)_2$ has transformed to MgF_2 ($E_{Mg\ 1s}$ = 1304.5 eV) [53] during ball milling. After dehydrogenation at 500 °C, the MgF_2 amount increases according to the XPS result in Fig. S15 (Supporting Information), confirming the further interaction of $Mg(BH_4)_2$ and F group on the Ti_2C surface. The deconvoluted Mg 1s spectrum of the dehydrogenated $Mg(BH_4)_2$-30Ti_2C exhibits four peaks centered at 1303.3, 1303.8, 1304.5 and 1305.3 eV, respectively, which are assigned to Mg metal [54], the combination of MgB_2 [55] and MgH_2 ($E_{Mg\ 1s}$ = 1303.7 eV obtained from Fig. S16, Supporting Information), MgF_2, and MgO [56], respectively. The B 1s spectrum could be fitted into four peaks located at 186.6, 187.2, 188.4 and 191.6 eV, which correspond to MgB_2, elemental boron, and B_xO_y respectively [55,57]. The above results prove that the surficial F groups and transition metal ions with high valences in the MXenes react with $Mg(BH_4)$ during the milling and dehydrogenation process, generating zero-valent transition metals, MgF_2, *etc*.

Hence, the second/third isothermal dehydrogenation tests at 260 °C were conducted to determine the reversible hydrogen storage properties of the $Mg(BH_4)_2$-30MXenes. As illustrated in Fig. 6a, the second/third dehydrogenation capacities of the $Mg(BH_4)_2$-30Ti_3C_2, $Mg(BH_4)_2$-30Ti_2C, and $Mg(BH_4)_2$-30Nb_2C composites within 360 min are 3.5/3.2, 3.6/3.3, 3.0/2.9 wt%, respectively, all being obviously lower compared with their initial hydrogen discharge capacities shown in Fig. 3c. The $Mg(BH_4)_2$-30Ti_2C exhibits the highest reversible capacities and the fastest H_2 release rate among the three composites. The structural evolution of $Mg(BH_4)_2$-30Ti_2C during the isothermal dehydrogenation and rehydrogenation process was specially studied through XRD, XPS, and FTIR characterizations. However, the information gained from the XRD patterns (Fig. S17, Supporting Information) of the first dehydrogenated and first rehydrogenated $Mg(BH_4)_2$-30Ti_2C is limited, as there is no visible difference in the two curves, in which only MgB_2 and Ti_2C phases could be detected. Therefore, XPS and FTIR were used to investigate whether Mg or Ti-related hydrides were produced after hydrogenation. From the

similar XPS results of Ti 2p for the two samples (Fig. S18, Supporting Information), The Ti_2C MXene as well as the polyvalent Ti ions (Ti^{4+}, Ti^{3+}, Ti^{2+}) and Ti metal on the surface remain unchanged from the dehydrogenation produces to the hydrogenation produces. It could be deduced from the XRD and XPS analyses that the metal titanium is not hydrogenated. FTIR spectra for the $Mg(BH_4)_2$-30Ti_2C after the first dehydrogenation (DEH1), the first hydrogenation (REH1), and the third dehydrogenation (DEH3) processes present obvious differences as shown in Fig. 6b. For the products of DEH1, multiple IR absorption peaks corresponding to B-H bonds in $Mg(BH_4)_2$ (stretching: 2366–2223 cm^{-1}, bending: 1262–1121 cm^{-1}), polyborane intermediates (~2465 cm^{-2}, 717–1025 cm^{-2}), and Mg-H bonds in MgH_2 (555 cm^{-2}) are detected as marked out in the profile, suggesting the incomplete decomposition of $Mg(BH_4)_2$-30Ti_2C under 260 °C. After hydrogenation at 300 °C, the absorption peaks at 2361 cm^{-1} and 555 cm^{-1} become stronger, showing increased amounts of $Mg(BH_4)_2$ and MgH_2. New strong peaks centered at 2246, 1238, 1105 and 991 cm^{-1} are detected by FTIR, which are ascribed to the B-H vibrations in polyborane intermediates or their combination with $Mg(BH_4)_2$. However, it is notoriously difficult to provide accurate assignments for the peaks owing to the highly complex decomposition mechanism of $Mg(BH_4)_2$. The result demonstrates that some hydrogen is absorbed and stored in $Mg(BH_4)_2$, polyborane intermediates, and MgH_2 during the rehydrogenation process. The hydrogen storage in the rehydrogenated sample is reversible, as the sample of DEH3 exhibits a similar FTIR spectrum to that of DEH1. The stronger peak of MgH_2 in the third dehydrogenated products suggests that the hydrogen release kinetics has slightly deteriorated with cycling, leading to a reduced H_2 release amount in the third dehydrogenation cycle of $Mg(BH_4)_2$-30Ti_2C. This phenomenon has also been observed in the cycling tests of $Mg(BH_4)_2$-30Ti_3C_2 and $Mg(BH_4)_2$-30Nb_2C. Nevertheless, their reversible hydrogen capacities and dehydrogenation rates are still superior to those of pure $Mg(BH_4)_2$ (1.5 wt%) in the first dehydrogenation.

According to the above-mentioned results, the three MXenes markedly improve the dehydriding properties of $Mg(BH_4)_2$. First, once $Mg(BH_4)_2$ comes into close contact with the MXene surfaces, strong electronic interactions occur at the interfaces, thus contributing to weakened bond energies between B and H. This is a crucial reason for the destabilization of $Mg(BH_4)_2$. Additionally, the plentiful high valence transition metals on the surfaces of MXenes react with the reductive $Mg(BH_4)_2$ during ball milling, resulting in the formations of Ti or Nb metal particles, which will become the active sites for catalysis [21]. Furthermore, that the abundant groups such as F on the surfaces of MXenes react with $Mg(BH_4)_2$ leads to the generation of stable MgF_2, which could accelerate the decomposition reaction of $Mg(BH_4)_2$. The above reactions take place during the dehydrogenation process as well, letting $Mg(BH_4)_2$ maintain a rapid desorption rate. The *in-situ* generated Ti or Nb particles distribute on the surfaces of lamellar MXenes, and keep in close contact with $Mg(BH_4)_2$ and MgF_2. Those phases constitute multiple interfaces, which provide excellent charge transfer and increased hydrogen diffusion channels, and thus facilitate the dehydrogenation of $Mg(BH_4)_2$ [45,58,59]. Besides, the $Mg(BH_4)_2$-30MXenes exhibit good reversible performances, although a reduction in reversible hydrogen capacity could be caused by the generations of MgF_2, MgO, and B_xO_y. The catalytic abilities of the MXenes therefore are related to both the carbides themselves and their surficial groups. Ti_2C is found to be the best catalyst among the three MXenes. However, there is still room for amelioration in the dehydriding performances of $Mg(BH_4)_2$. Moreover, reducing the Ti_2C addition amount on the premise of an excellent catalyzing effect is another important aspect. Our subsequent studies will focus on the engineering strategies of Ti_2C MXene to achieve better catalytic performances in the hydrogen storage of $Mg(BH_4)_2$.

4. Conclusions

In summary, the catalytic effects of multiple transition metal carbides (Ti_3C_2, Ti_2C, Nb_2C) on the hydrogen storage performance of $Mg(BH_4)_2$ have been studied. The $Mg(BH_4)_2$-30MXene (Ti_3C_2, Ti_2C, Nb_2C) composites show the reduced initial dehydrogenation temperatures of 149, 132 and 141 °C, the increased isothermal dehydrogenation amounts of 8.7, 10.2 and 7.9 wt% within 360 min under 260 °C, and the decreased dehydriding apparent activation energies of 72.91, 41.82 and 106.17 kJ mol^{-1}, respectively, compared with those of pure $Mg(BH_4)_2$. This means that the MXenes could catalyze the dehydrogenation reactions of $Mg(BH_4)_2$ and significantly enhance the dehydriding kinetics, with the catalytic effects of the three MXenes ranked in the following order: Ti_2C > Ti_3C_2 > Nb_2C. The catalytic effects could mainly be ascribed to two points through DFT calculations and structural characterizations: i) the interfacial charge transfer between $Mg(BH_4)_2$ and MXenes, and the dehybridization of B and H orbitals weakening the B-H bond strengths in $[BH_4]^-$; ii) the multiphase interfaces consisting of MXenes, transition metal particles, $Mg(BH_4)_2$, and MgF_2, *etc*., due to the interactions between MXenes and $Mg(BH_4)_2$ facilitating the charge transfer, accelerating the breakdown of B-H bonds, and increasing the diffusion channels for hydrogen. In addition, the MXenes are also found to be beneficial in improving the reversibility of $Mg(BH_4)_2$. This study may arouse some interest and provide some ideas in the selection of catalysts with novel structures for improving the hydrogen storage properties of $Mg(BH_4)_2$.

Declaration of Competing Interest

The authors declare that they have no known competing financial interests or personal relationships that could have appeared to influence the work reported in this paper.

Data availability

Data will be made available on request.

Acknowledgments

This work was supported by the National Key Research and Development Plan (2021YFB3802400), the National Natural Science Foundation of China (Grant no. 52071141, 52201250, 52271212), and Interdisciplinary Innovation Program of North China Electric Power University (Grant no. XM2112355).

Appendix A. Supplementary data

Supplementary data to this article can be found online at https://doi.org/10.1016/j.cej.2023.147387.

References

[1] M. Asif, S.S. Bibi, S. Ahmed, M. Irshad, M.S. Hussain, H. Zeb, M.K. Khan, J. Kim, Recent advances in green hydrogen production, storage and commercial-scale use via catalytic ammonia cracking, Chem. Eng. J. 473 (2023), 145381, https://doi.org/10.1016/j.cej.2023.145381.

[2] L. Ren, Y. Li, N. Zhang, Z. Li, X. Lin, W. Zhu, C. Lu, W. Ding, J. Zou, Nanostructuring of Mg-based hydrogen storage materials: Recent advances for promoting key applications, Nano-Micro Lett. 15 (2023) 93, https://doi.org/10.1007/s40820-023-01041-5.

[3] G. Singh, K. Ramadass, V.D.B.C. DasiReddy, X. Yuan, Y.S. Ok, N. Bolan, X. Xiao, T. Ma, A. Karakoti, J. Yi, A. Vinu, Material-based generation, storage, and utilisation of hydrogen, Prog. Mater. Sci. 135 (2023), 101104, https://doi.org/10.1016/j.pmatsci.2023.101104.

[4] Z. Chen, K.O. Kirlikovali, K.B. Idrees, M.C. Wasson, O.K. Farha, Porous materials for hydrogen storage, Chem 8 (2022) 693–716, https://doi.org/10.1016/j.chempr.2022.01.012.

[5] J. Zheng, C.-G. Wang, H. Zhou, E. Ye, J. Xu, Z. Li, X.J. Loh, Current research trends and perspectives on solid-state nanomaterials in hydrogen storage, Research 2021 (2021), https://doi.org/10.34133/2021/3750689.

[6] M.A.N. Ahmad, N. Sazelee, N.A. Ali, M. Ismail, An overview of the recent advances of additive-improved $Mg(BH_4)_2$ for solid-state hydrogen storage material, Energies 15 (2022) 862, https://doi.org/10.3390/en15030862.

[7] Z. Jiang, J. Yuan, H. Han, Y. Wu, Effect of carbon nanotubes on the microstructural evolution and hydrogen storage properties of $Mg(BH_4)_2$, J. Alloy. Compd. 743 (2018) 11–16, https://doi.org/10.1016/j.jallcom.2018.01.346.

[8] X. Wang, X. Xiao, J. Zheng, Z. Yao, M. Zhang, X. Huang, L. Chen, Insights into magnesium borohydride dehydrogenation mechanism from its partial reversibility under moderate conditions, Mater. Today Energy 18 (2020), 100552, https://doi.org/10.1016/j.mtener.2020.100552.

[9] J. Yuan, H. Huang, Z. Jiang, Y. Lv, B. Liu, B. Zhang, Y. Yan, Y. Wu, Ni-Doped carbon nanotube-$Mg(BH_4)_2$ composites for hydrogen storage, ACS Appl. Nano Mater. 4 (2021) 1604–1612, https://doi.org/10.1021/acsanm.0c02738.

[10] Y. Liu, W. Zhang, X. Zhang, L. Yang, Z. Huang, F. Fang, W. Sun, M. Gao, H. Pan, Nanostructured light metal hydride: Fabrication strategies and hydrogen storage performance, Renew. Sust. Energy Rev. 184 (2023), 113560, https://doi.org/10.1016/j.rser.2023.113560.

[11] J. Zheng, H. Cheng, X. Wang, M. Chen, X. Xiao, L. Chen, $LiAlH_4$ as a "microlighter" on the fluorographite surface triggering the dehydrogenation of $Mg(BH_4)_2$: Toward more than 7 wt % hydrogen release below 70 °C, ACS Appl. Energy Mater. 3 (2020) 3033–3041, https://doi.org/10.1021/acsaem.0c00134.

[12] J. Zheng, X. Xiao, L. Zhang, Y. He, S. Li, H. Ge, L. Chen, Study on the dehydrogenation properties and reversibility of $Mg(BH_4)_2$-AlH_3 composite under moderate conditions, Int. J. Hydrogen Energy 42 (2017) 8050–8056, https://doi.org/10.1016/j.ijhydene.2016.12.045.

[13] H. Huang, B. Liu, Y. Lv, W. Lv, J. Yuan, Y. Wu, Double regulation of $Mg_{95}Ni_5$ hydride in suppressing ammonia and promoting hydrogen evolution for Mg $(BH_4)_2{\cdot}2NH_3$, J. Alloy. Compd. 901 (2022), 163468, https://doi.org/10.1016/j.jallcom.2021.163468.

[14] Y. Lv, B. Zhang, H. Huang, B. Liu, W. Lv, J. Yuan, G. Xia, X. Yu, D. Sun, Y. Wu, Niobium fluoride-modified hydrogen evolution reaction of magnesium borohydride diammoniate, J. Mater. Sci. Technol. 156 (2023) 197–205, https://doi.org/10.1016/j.jmst.2023.01.030.

[15] Y. Lv, Y. Wu, Current research progress in magnesium borohydride for hydrogen storage (A review), Prog. Nat. Sci.-Mater. 31 (2021) 809–820, https://doi.org/10.1016/j.pnsc.2021.11.001.

[16] E.G. Bardají, N. Hanada, O. Zabara, M. Fichtner, Effect of several metal chlorides on the thermal decomposition behaviour of α-$Mg(BH_4)_2$, Int. J. Hydrogen Energy 36 (2011) 12313–12318, https://doi.org/10.1016/j.ijhydene.2011.07.008.

[17] A. Al-Kukhun, H.T. Hwang, A. Varma, NbF_5 additive improves hydrogen release from magnesium borohydride, Int. J. Hydrogen Energy 37 (2012) 17671–17677, https://doi.org/10.1016/j.ijhydene.2012.09.097.

[18] X. Wang, X. Xiao, J. Zheng, X. Huang, M. Chen, L. Chen, In-situ synthesis of amorphous $Mg(BH_4)_2$ and chloride composite modified by NbF_5 for superior reversible hydrogen storage properties, Int. J. Hydrogen Energy 45 (2020) 2044–2053, https://doi.org/10.1016/j.ijhydene.2019.11.023.

[19] N.N. Sulaiman, M. Ismail, S.N. Timmiati, K.L. Lim, Improved hydrogen storage performances of $LiAlH_4$ + $Mg(BH_4)_2$ composite with TiF_3 addition, Int. J. Energy Res. 45 (2021) 2882–2898, https://doi.org/10.1002/er.5984.

[20] X. Wang, X. Xiao, J. Zheng, Z. Hang, W. Lin, Z. Yao, M. Zhang, L. Chen, The dehydrogenation kinetics and reversibility improvements of $Mg(BH_4)_2$ doped with Ti nano-particles under mild conditions, Int. J. Hydrogen Energy 46 (2021) 23737–23747, https://doi.org/10.1016/j.ijhydene.2021.04.149.

[21] J. Zheng, H. Cheng, X. Xiao, M. Chen, L. Chen, Enhanced low temperature hydrogen desorption properties and mechanism of $Mg(BH_4)_2$ composited with 2D MXene, Int. J. Hydrogen Energy 44 (2019) 24292–24300, https://doi.org/10.1016/j.ijhydene.2019.07.177.

[22] Y. Fan, D. Chen, X. Liu, G. Fan, B. Liu, Improving the hydrogen storage performance of lithium borohydride by Ti_3C_2 MXene, Int. J. Hydrogen Energy 44 (2019) 29297–29303, https://doi.org/10.1016/j.ijhydene.2019.01.011.

[23] K. Ren, B. Wang, Revealing the effect of 2D carbides with different metal sites for improving hydrogen storage in MgH_2, Front. Chem. 10 (2022) 1000408, https://doi.org/10.3389/fchem.2022.1000408.

[24] H. Liu, S. He, G. Li, Y. Wang, L. Xu, P. Sheng, X. Wang, T. Jiang, C. Huang, Z. Lan, W. Zhou, J. Guo, Directed stabilization by air-milling and catalyzed decomposition by layered titanium carbide toward low-temperature and high-capacity hydrogen storage of aluminum hydride, ACS Appl. Mater. Interfaces 14 (2022) 42102–42112, https://doi.org/10.1021/acsami.2c11805.

[25] H. Gao, R. Shi, Y. Liu, Y. Zhu, J. Zhang, L. Li, X. Hu, Facet-dependent catalytic activity of two-dimensional $Ti_3C_2T_x$ MXene on hydrogen storage performance of MgH_2, J. Magnes. Alloy. (2022), https://doi.org/10.1016/j.jma.2022.02.006.

[26] C. Lu, H. Liu, L. Xu, H. Luo, S. He, X. Duan, X. Huang, X. Wang, Z. Lan, J. Guo, Two-dimensional vanadium carbide for simultaneously tailoring the hydrogen sorption thermodynamics and kinetics of magnesium hydride, J. Magnes. Alloy. 10 (2022) 1051–1065, https://doi.org/10.1016/j.jma.2021.03.030.

[27] H. Liu, X. Duan, Z. Wu, H. Luo, X. Wang, C. Huang, Z. Lan, W. Zhou, J. Guo, M. Ismail, Exfoliation of compact layered Ti_2VAlC_2 MAX to open layered Ti_2VC_2 MXene towards enhancing the hydrogen storage properties of MgH_2, Chem. Eng. J. 468 (2023), 143688, https://doi.org/10.1016/j.cej.2023.143688.

[28] R. Wu, H. Du, Z. Wang, M. Gao, H. Pan, Y. Liu, Remarkably improved hydrogen storage properties of $NaAlH_4$ doped with 2D titanium carbide, J. Power Sources 327 (2016) 519–525, https://doi.org/10.1016/j.jpowsour.2016.07.095.

[29] X. Feng, J. Yuan, Y. Lv, B. Liu, H. Huang, B. Zhang, Y. Yan, S. Han, Y. Wu, Improvement of desorption performance of $Mg(BH_4)_2$ by two-dimensional Ti_3C_2 MXene addition, Int. J. Hydrogen Energy 45 (2020) 16654–16662, https://doi.org/10.1016/j.ijhydene.2020.04.132.

[30] X. Kang, Z. Fang, L. Kong, H. Cheng, X. Yao, G. Lu, P. Wang, Ammonia borane destabilized by lithium hydride: An advanced on-board hydrogen storage material, Adv. Mater. 20 (2008) 2756–2759, https://doi.org/10.1002/adma.200702958.

[31] G. Kresse, J. Furthmüller, Efficiency of ab-initio total energy calculations for metals and semiconductors using a plane-wave basis set, Comput. Mater. Sci. 6 (1996) 15–50, https://doi.org/10.1016/0927-0256(96)00008-0.

[32] G. Kresse, D. Joubert, From ultrasoft pseudopotentials to the projector augmented-wave method, Phys. Rev. B 59 (1999) 1758–1775, https://doi.org/10.1103/PhysRevB.59.1758.

[33] J.P. Perdew, K. Burke, M. Ernzerhof, Generalized gradient approximation made simple, Phys. Rev. Lett. 77 (1996) 3865–3868, https://doi.org/10.1103/physrevlett.77.3865.

[34] W. Tang, E. Sanville, G. Henkelman, A grid-based Bader analysis algorithm without lattice bias, J. Phys.: Condens. Matter 21 (2009), 084204, https://doi.org/10.1088/0953-8984/21/8/084204.

[35] E. Aydin, J.K. El-Demellawi, E. Yarali, F. Aljamaan, S. Sansoni, A. ur Rehman, G. Harrison, J. Kang, A.E. Labban, M.D. Bastiani, A. Razzaq, E.V. Kerschaver, T. G. Allen, O.F. Mohammed, T. Anthopoulos, H.N. Alshareef, S.D. Wolf, Scaled deposition of $Ti_3C_2T_x$ MXene on compleces for silicon heterojunction solar cells, ACS nano 16 (2022) 2419–2428, https://doi.org/10.1021/acsnano.1c08871.

[36] L. Ding, Y. Wei, Y. Wang, H. Chen, J. Caro, H. Wang, A two-dimensional lamellar membrane: MXene nanosheet stacks, Angew. Chem. Int. Ed. 56 (2017) 1825–1829, https://doi.org/10.1002/anie.201609306.

[37] Y. Guan, R. Zhao, Y. Cong, K. Chen, J. Wu, H. Zhu, Z. Dong, Q. Zhang, G. Yuan, Y. Li, J. Zhang, X. Li, Flexible Ti_2C MXene film: Synthesis, electrochemical performance and capacitance behavior, Chem. Eng. J. 433 (2022), 133582, https://doi.org/10.1016/j.cej.2021.133582.

[38] S. Tu, F. Ming, J. Zhang, X. Zhang, H.N. Alshareef, MXene-derived ferroelectric crystals, Adv. Mater. 31 (2019) 1806860, https://doi.org/10.1002/adma.201806860.

[39] X. Li, X. Ma, Y. Hou, Z. Zhang, Y. Lu, Z. Huang, G. Liang, M. Li, Q. Yang, J. Ma, N. Li, B. Dong, Q. Huang, F. Chen, J. Fan, C. Zhi, Intrinsic voltage plateau of a Nb_2CT_x MXene cathode in an aqueous electrolyte induced by high-voltage scanning, Joule 5 (2021) 2993–3005, https://doi.org/10.1016/j.joule.2021.09.006.

[40] J.-H. Her, P.W. Stephens, Y. Gao, G.L. Soloveichik, J. Rijssenbeek, M. Andrus, J.-C. Zhao, Structure of unsolvated magnesium borohydride $Mg(BH_4)_2$, Acta Crystallogr. B 63 (2007) 561–568, https://doi.org/10.1107/s0108768107022665.

[41] H.-W. Li, K. Kikuchi, Y. Nakamori, K. Miwa, S. Towata, S. Orimo, Effects of ball milling and additives on dehydriding behaviors of well-crystallized $Mg(BH_4)_2$, Scripta Mater. 57 (2007) 679–682, https://doi.org/10.1016/j.scriptamat.2007.06.052.

[42] K. Chłopek, C. Frommen, A. Léon, O. Zabara, M. Fichtner, Synthesis and properties of magnesium tetrahydroborate, $Mg(BH_4)_2$, J. Mater. Chem. 17 (2007) 3496–3503, https://doi.org/10.1039/B702723K.

[43] Q. Wang, Z. Li, H. Deng, Y. Chen, Y. Yan, Enhanced interface stability of ammine magnesium borohydride by in situ decoration of $MgBr_2{\cdot}2NH_3$ nanoparticles, Chem. Communs. 59 (2023) 6726–6729, https://doi.org/10.1039/D3CC00994G.

[44] M. Luo, J. Tian, S. Liu, W. Zhang, An integrated photothermal-photocatalytic materials for efficient photocatalytic performance boosting by synergistic photothermally, Appl. Surf. Sci. 593 (2022), 153382, https://doi.org/10.1016/j.apsusc.2022.153382.

[45] Z. Zhang, D. Gao, J. Zheng, A. Xia, Q. Zhang, Li Wang, L. Zhang, Heterostructured VF_4@Ti_3C_2 catalyst improving reversible hydrogen storage properties of $Mg(BH_4)_2$, Chem. Eng. J. 460 (2023) 141690, https://doi.org/10.1016/j.cej.2023.141690.

[46] Y. Xia, H. Zhang, Y. Sun, L. Sun, F. Xu, S. Sun, G. Zhang, P. Huang, Y. Du, J. Wang, S.P. Verevkin, A.A. Pimerzin, Dehybridization effect in improved dehydrogenation of $LiAlH_4$ by doping with two-dimensional Ti_3C_2, Mater. Today Nano 8 (2019), 100054, https://doi.org/10.1016/j.mtnano.2019.100054.

[47] Y. Zhu, S. Shen, L. Ouyang, J. Liu, H. Wang, Z. Huang, M. Zhu, Effective synthesis of magnesium borohydride *via* B-O to B-H bond conversion, Chem. Eng. J. 432 (2022), 134322, https://doi.org/10.1016/j.cej.2021.134322.

[48] J.G. Vitillo, S. Bordiga, M. Baricco, Spectroscopic and structural characterization of thermal decomposition of γ-$Mg(BH_4)_2$: Dynamic vacuum versus H_2 atmosphere, J. Phys. Chem. C 119 (2015) 25340–25351, https://doi.org/10.1021/acs.jpcc.5b06806.

[49] R. Meng, J. Huang, Y. Feng, L. Zu, C. Peng, L. Zheng, L. Zheng, Z. Chen, G. Liu, B. Chen, Y. Mi, J. Yang, Black phosphorus quantum dot/Ti_3C_2 MXene nanosheet composites for efficient electrochemical lithium/sodium-ion storage, Adv. Energy Mater. 8 (2018) 1801514, https://doi.org/10.1002/aenm.201801514.

[50] M. Chen, Q. Zhang, F. Xu, Z. Li, J. Li, W. Wang, S. Wang, M. Wang, T. Qiu, J. Li, H. Zhang, W. Wang, Ti_3C_2 and Ti_2C MXene materials for high-performance isolation of extracellular vesicles *via* coprecipitation, Anal. Chim. Acta 1269 (2023), 341426, https://doi.org/10.1016/j.aca.2023.341426.

[51] M.C. Biesinger, L.W.M. Lau, A.R. Gerson, R.St.C. Smart, Resolving surface chemical states in XPS analysis of first row transition metals, oxides and hydroxides: Sc, Ti, V, Cu and Zn, Appl. Surf. Sci. 257 (2010) 887–898, https://doi.org/10.1016/j.apsusc.2010.07.086.

[52] H. Ding, Y. Li, M. Li, K. Chen, K. Liang, G. Chen, J. Lu, J. Palisaitis, P.O.Å. Persson, P. Eklund, L. Hultman, S. Du, Z. Chai, Y. Gogotsi, Q. Huang, Chemical scissor-mediated structural editing of layered transition metal carbides, Science 379 (2023) 1130–1135, https://doi.org/10.1126/science.add5901.

[53] J.Y. Kim, G. Liu, R.E.A. Ardhi, J. Park, H. Kim, J.K. Lee, Stable Zn metal anodes with limited Zn-doping in MgF_2 interphase for fast and uniformly ionic flux, Nano-Micro Lett. 14 (2022) 46, https://doi.org/10.1007/s40820-021-00788-z.

[54] L.-L. Kong, L. Wang, Z.-C. Ni, S. Liu, G.-R. Li, X.-P. Gao, Lithium-magnesium alloy as a stable anode for lithium-sulfur battery, Adv. Funct. Mater. 29 (2019) 1808756, https://doi.org/10.1002/adfm.201808756.

[55] H. Gunda, K.G. Ray, L.E. Klebanoff, C. Dun, M.A.T. Marple, S. Li, P. Sharma, R. W. Friddle, J.D. Sugar, J.L. Snider, R.D. Horton, B.C. Davis, J.M. Chames, Y.-S. Liu, J. Guo, H.E. Mason, J.J. Urban, B.C. Wood, M.D. Allendorf, K. Jasuja, V. Stavila, Hydrogen storage in partially exfoliated magnesium diboride multilayers, Small 19 (2023) 2205487, https://doi.org/10.1002/smll.202205487.

[56] N. Yan, X. Lu, Z. Lu, H. Yu, F. Wu, J. Zheng, X. Wang, L. Zhang, Enhanced hydrogen storage properties of Mg by the synergistic effect of grain refinement and $NiTiO_3$ nanoparticles, J. Magnes. Alloy. 10 (2022) 3542–3552, https://doi.org/10.1016/j.jma.2021.03.014.

[57] C.W. Ong, H. Huang, B. Zheng, R.W.M. Kwok, Y.Y. Hui, W.M. Lau, X-ray photoemission spectroscopy of nonmetallic materials: Electronic structures of boron and B_xO_y, J. Appl. Phys. 95 (2004) 3527–3534, https://doi.org/10.1063/1.1651321.

[58] X. Zhang, Y. Sun, S. Ju, J. Ye, X. Hu, W. Chen, L. Yao, G. Xia, F. Fang, D. Sun, X. Yu, Solar-driven reversible hydrogen storage, Adv. Mater 35 (2023) 2206946, https://doi.org/10.1002/adma.202206946.

[59] Z. Wang, X. Zhang, Z. Ren, Y. Liu, J. Hu, H. Li, M. Gao, H. Pan, Y. Liu, In situ formed ultrafine NbTi nanocrystals from a NbTiC solid-solution MXene for hydrogen storage in MgH_2, J. Mater. Chem. A 7 (2019) 14244, https://doi.org/10.1039/c9ta03665b.